



Millimeter-wave Interferometric Sensing

by Charles R. Dietlein, Amir Zaghoul, and David A. Wikner

ARL-TR-5668

September 2011

NOTICES

Disclaimers

The findings in this report are not to be construed as an official Department of the Army position unless so designated by other authorized documents.

Citation of manufacturer's or trade names does not constitute an official endorsement or approval of the use thereof.

Destroy this report when it is no longer needed. Do not return it to the originator.

Army Research Laboratory

Adelphi, MD 20783-1197

ARL-TR-5668

September 2011

Millimeter-wave Interferometric Sensing

Charles R. Dietlein, Amir Zaghoul, and David A. Wikner
Sensors and Electron Devices Directorate, ARL

REPORT DOCUMENTATION PAGE

Form Approved
OMB No. 0704-0188

Public reporting burden for this collection of information is estimated to average 1 hour per response, including the time for reviewing instructions, searching existing data sources, gathering and maintaining the data needed, and completing and reviewing the collection information. Send comments regarding this burden estimate or any other aspect of this collection of information, including suggestions for reducing the burden, to Department of Defense, Washington Headquarters Services, Directorate for Information Operations and Reports (0704-0188), 1215 Jefferson Davis Highway, Suite 1204, Arlington, VA 22202-4302. Respondents should be aware that notwithstanding any other provision of law, no person shall be subject to any penalty for failing to comply with a collection of information if it does not display a currently valid OMB control number.

PLEASE DO NOT RETURN YOUR FORM TO THE ABOVE ADDRESS.

1. REPORT DATE (DD-MM-YYYY) September 2011	2. REPORT TYPE Final	3. DATES COVERED (From - To) March to June 2010	
4. TITLE AND SUBTITLE Millimeter-wave Interferometric Sensing		5a. CONTRACT NUMBER	
		5b. GRANT NUMBER	
		5c. PROGRAM ELEMENT NUMBER	
6. AUTHOR(S) Charles R. Dietlein, Amir Zaghoul, and David A. Wikner		5d. PROJECT NUMBER	
		5e. TASK NUMBER	
		5f. WORK UNIT NUMBER	
7. PERFORMING ORGANIZATION NAME(S) AND ADDRESS(ES) U.S. Army Research Laboratory ATTN: RDRL-SER-M 2800 Powder Mill Road Adelphi, MD 20783-1197		8. PERFORMING ORGANIZATION REPORT NUMBER ARL-TR-5668	
9. SPONSORING/MONITORING AGENCY NAME(S) AND ADDRESS(ES)		10. SPONSOR/MONITOR'S ACRONYM(S)	
		11. SPONSOR/MONITOR'S REPORT NUMBER(S)	
12. DISTRIBUTION/AVAILABILITY STATEMENT Approved for public release; distribution unlimited.			
13. SUPPLEMENTARY NOTES			
14. ABSTRACT This report explores the feasibility of short-range ground-based millimeter-wave sensing systems based on interferometric imaging techniques. In comparison with infrared and visible wavelength focal-plane arrays (FPA), millimeter-wave FPAs always have fewer detectors and image pixels, poorer spatial resolution, lower signal-to-noise ratio, and an increase of illumination-based artifacts such as glint in the images. Calibration and scanning schemes induce additional complications. These difficulties are ultimately a consequence of the millimeter-wave's much longer wavelengths compared to visible or infrared frequencies. This research effort addresses a specific limitation: low-detector-count FPAs. An alternative approach to traditional, high-detector-count, staring FPAs is interferometric (coherence) imaging, wherein an array with a low number of coherent detectors is exploited to reconstruct the field distribution in the object plane. This interferometric approach is used extensively by radio astronomers at lower frequencies. In this report, we study this technique's validity at 220 GHz for imaging terrestrial scenes.			
15. SUBJECT TERMS Millimeter-wave, imaging, coherence, interferometry, standoff			
16. SECURITY CLASSIFICATION OF:			17. LIMITATION OF ABSTRACT UU
a. REPORT Unclassified	b. ABSTRACT Unclassified	c. THIS PAGE Unclassified	
			18. NUMBER OF PAGES 20
19a. NAME OF RESPONSIBLE PERSON Charles R. Dietlein			
			19b. TELEPHONE NUMBER (Include area code) (301) 394-1523

Contents

List of Figures	iv
Summary	1
1. Introduction	3
2. Methods, Assumptions, and Procedures	3
3. Results and Discussion	6
4. Conclusions	11
5. References	12
Distribution List	13

List of Figures

Figure 1. Geometry illustrating the van Cittert-Zernike theorem discussed in the text.....	4
Figure 2. Plot of phase difference between detectors for various array sizes (shown in the legend in units of meters), as a function of range between the array and object planes. Frequency was fixed at 220 GHz. The phase differences $\phi_\delta \ll 1$ imply a paraxial approximation. The black square indicates where the experiments and simulations in this report were performed.....	6
Figure 3. (Left) Array geometry showing 32 detector positions arranged in a spiral configuration, and (right) sampling in the uv plane.....	7
Figure 4. (Left) A histogram containing the uv plane coverage shown in Cartesian coordinates in figure 3 (right). The histogram contains 496 samples in 50 bins. (Right) A histogram showing uv plane coverage for a rectangularly-gridded array, with approximately the same number of detectors and physical size as that of figure 3 (left).....	8
Figure 5. (Left) Reconstruction of the simulated point source at a range of 0.5 m from the spiral array, and (right) best-fit 2-D Gaussian (opaque surface) with the reconstructed object plane (mesh surface), for purposes of determining the FWHM of the point source.....	9
Figure 6. (Left) Reconstruction of the two simulated point sources at a range of 0.5 m from the spiral array, and (right) best-fit 2-D Gaussians (opaque surface) with the reconstructed object plane (mesh surface).....	9
Figure 7. Measured electric field amplitude pattern of two waveguide aperture sources. Range to the sources is approximately 0.5 m, and they are separated by approximately 6 cm. The fringes are tilted slightly, as the sources were not perfectly aligned with the y -axis. The nominal positions of the modeled detectors are depicted by the overlaid dots.....	10
Figure 8. (Left) Measured data, reconstructed electric field distribution at object plane and (right) simulation results with geometry matching the experimental setup.....	11

Summary

Millimeter-wave sensing systems designed for imaging almost always produce inferior images compared to their infrared and visible wavelength counterparts for a variety of fundamental reasons. These reasons include low detector/pixel count, poor signal-to-noise ratio, artifacts introduced by illumination, and issues arising from calibration or scanning schemes. This research effort is intended to address the issue of low-detector-count focal-plane arrays (FPA). Radio astronomers have dealt with this issue for many decades by using interferometry, or coherence imaging. This report details how interferometric imaging techniques can be used in the millimeter-wave regime for terrestrial applications.

INTENTIONALLY LEFT BLANK.

1. Introduction

This research effort explores, through computer simulations and experimental verification, the viability of interferometric techniques for millimeter-wave imaging. A fundamental limitation in millimeter-wave/terahertz imaging is the lack of high-detector-count FPAs. However, in the radio frequency through terahertz regime, coherent (phase-sensitive) detectors are available. Infrared and visible images are acquired with direct (amplitude-only) detectors. Coherent measurement of the incident electric field provides additional information regarding the spatial amplitude distribution in the object plane. The scope of this research is to explore an interferometric imaging array geometry with the goal of demonstrating that a sparsely populated coherent array can achieve comparable spatial resolution to that achieved by a traditional direct-detection fully populated FPA with similar physical dimensions. The computer program MATLAB® is employed to simulate the image amplitude distribution and quantify the spatial resolution of the array, and a table-top experiment is configured to verify the simulations.

2. Methods, Assumptions, and Procedures

An imaging interferometer consists of N coherent detectors arranged in an array; we will consider planar arrays for simplicity. Each detector measures the amplitude and phase of the incident radiation, while each pair of detectors measures one spatial Fourier component of the incident radiation. The specific spatial component is defined by the pair's physical separation, called a baseline. For N detectors, there are

$$p \equiv \binom{N}{2} = \frac{N^2 - N}{2} \quad (1)$$

unique 2-combinations. Each spatial Fourier component is represented by a single point in the Fourier plane, known as the uv plane. Image quality is usually determined by the uv plane sampling. Since each baseline measures a single spatial frequency, the optimum array geometry contains no redundant spacings. Typical geometries include a logarithmically spaced one-dimensional (1-D) array, or a spiral two-dimensional (2-D) array. While image quality is primarily dependent on uv plane sampling, it can be improved via standard reconstruction post-processing algorithms that are used by radio astronomers.

The van Cittert-Zernike theorem explains the fundamentals of interferometric imaging. A more detailed version of this discussion can be found in many textbooks (*1*). Briefly, a source of electromagnetic radiation occupies the infinitesimal surface dS' on the $z = 0$ plane, at xy

coordinates $x = x'$ and $y = y'$. A_0 is the amplitude of the source. An array of detectors is in the xy plane at $z = Z_0$. This geometry is illustrated in figure 1.

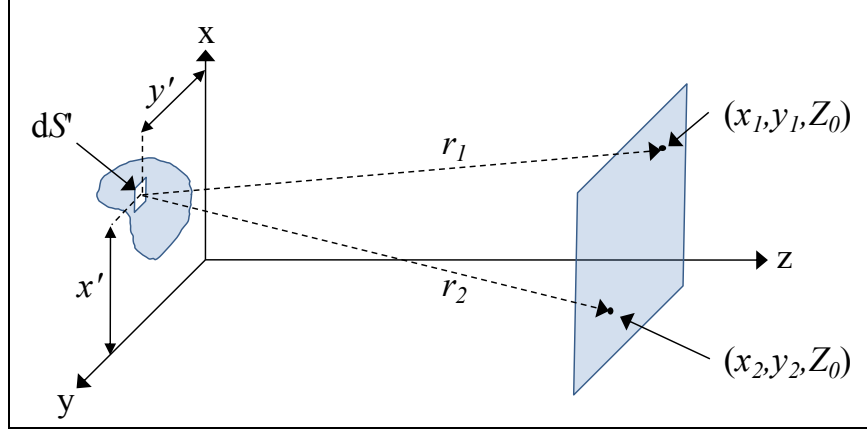


Figure 1. Geometry illustrating the van Cittert-Zernike theorem discussed in the text.

For a pair of detectors at (x_1, y_1, Z_0) and (x_2, y_2, Z_0) , the contributions to the total electric field provided by the source dS' can be expressed by

$$dE_1 = (A_0 / r_1) \exp(j\omega t - jkr_1) dS' \quad (2)$$

and

$$dE_2 = (A_0 / r_2) \exp(j\omega t - jkr_2) dS', \quad (3)$$

where $r_j = [(x' - x_j)^2 + (y' - y_j)^2 + Z_0^2]^{1/2}$ and $k = 2\pi / \lambda$. The mutual coherence function of the electric field at detector positions (x_1, y_1, Z_0) and (x_2, y_2, Z_0) is given by

$$C_{1,2} = \int_S \frac{\sigma_E(x', y') \exp[jk(r_1 - r_2)]}{r_1 r_2} dS', \quad (4)$$

where σ_E is the object plane amplitude distribution, and in the paraxial approximation,

$$r_1 - r_2 = \frac{(x_1^2 + y_1^2) - (x_2^2 + y_2^2)}{2Z_0} - \frac{(x_1 - x_2)x' + (y_1 - y_2)y'}{Z_0}. \quad (5)$$

The phase difference between a pair of detectors in a planar array, due to wave-front curvature, is given by

$$\phi_\delta = \frac{k[(x_1^2 + y_1^2) - (x_2^2 + y_2^2)]}{2Z_0}. \quad (6)$$

If we define the baselines $u = x_1 - x_2$ and $v = y_1 - y_2$, along with the angular coordinates $\xi = x'/Z_0$, $\eta = y'/Z_0$ and the approximation $1/r_1 r_2 \approx Z_0^{-2}$, the mutual coherence function can be written as (2)

$$C_{1,2}(u, v) = \exp(j\phi_\delta) \int_{-\infty-\infty}^{\infty} \int_{-\infty-\infty}^{\infty} \sigma_E(\xi, \eta) \exp[-jk(u\xi + v\eta)] d\xi d\eta. \quad (7)$$

When the phase shift $\exp(j\phi_\delta)$ can be ignored, the mutual coherence function above relates the coherence in the array plane to the amplitude distribution in the object plane via a Fourier transform. When the phase shift is significant, the correction based on the array geometry and distance to the object plane can be performed by adding a term to the measured phase at each detector, before computing the correlation function per baseline, $C_l = A_l \exp(j\Delta\phi_l)$. In the correlation function, $A_l = E_m E_n$ is the product of the measured field amplitudes at detectors m and n , and $\Delta\phi_l = \phi_m - \phi_n$ is the difference in phase between the two detectors.

For common array sizes in the millimeter-wave/terahertz frequency range, imaging at realistic ranges, the far-field condition of $\phi_\delta \ll 1$ is not met, and ϕ_δ must be adjusted in software after measurement. The relationship between range, array size, and phase shift is shown in figure 2. One may ask why we use the van Cittert-Zernike theorem, strictly valid only in the paraxial approximation, when we are in at least one of the three near-field conditions (3). The reason is that the paraxial approximation provides a useful form of the coherence function, because σ_E can be reconstructed easily through Fourier inversion. Reconstruction of the amplitude distribution from the correlation function of each baseline is performed by

$$\sigma_E(\xi, \eta) = \sum_{l=1}^p \{\Re(C_l) \cos[k(u_l \xi + v_l \eta)] - \Im(C_l) \sin[k(u_l \xi + v_l \eta)]\}.$$

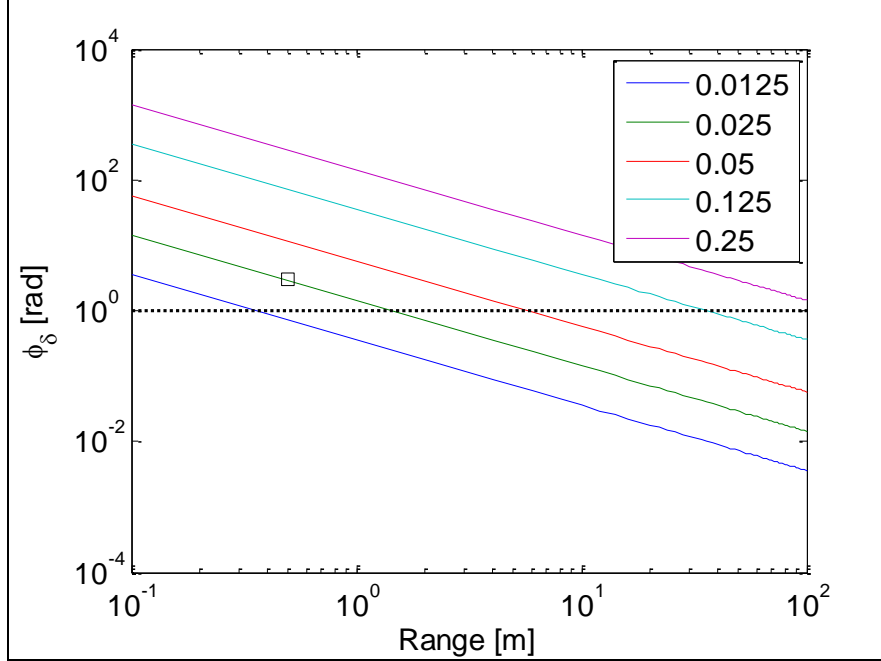


Figure 2. Plot of phase difference between detectors for various array sizes (shown in the legend in units of meters), as a function of range between the array and object planes. Frequency was fixed at 220 GHz. The phase differences $\phi_\delta \ll 1$ imply a paraxial approximation. The black square indicates where the experiments and simulations in this report were performed.

3. Results and Discussion

We focused our efforts around $f = 220$ GHz, primarily because it is one of the few bands with an acceptable atmospheric transmission window above $f = 100$ GHz. Additionally, the wavelength of approximately $\lambda = 1.4$ mm provides adequate spatial resolution for a variety of tasks with moderate array sizes. Finally, it is easy to find commercial hardware that operates at this frequency. While this approach will work at arbitrary ranges, we constrained our simulations to those that could be replicated on a laboratory bench with off-the-shelf equipment. We chose a range of approximately 0.5 m and an array size of approximately 20 mm^2 . Figure 3 (left) shows one of the simulated array geometries we explored, a planar Archimedean spiral, with $N = 32$ detectors. The array's sampling in the uv plane is shown in figure 3 (right).

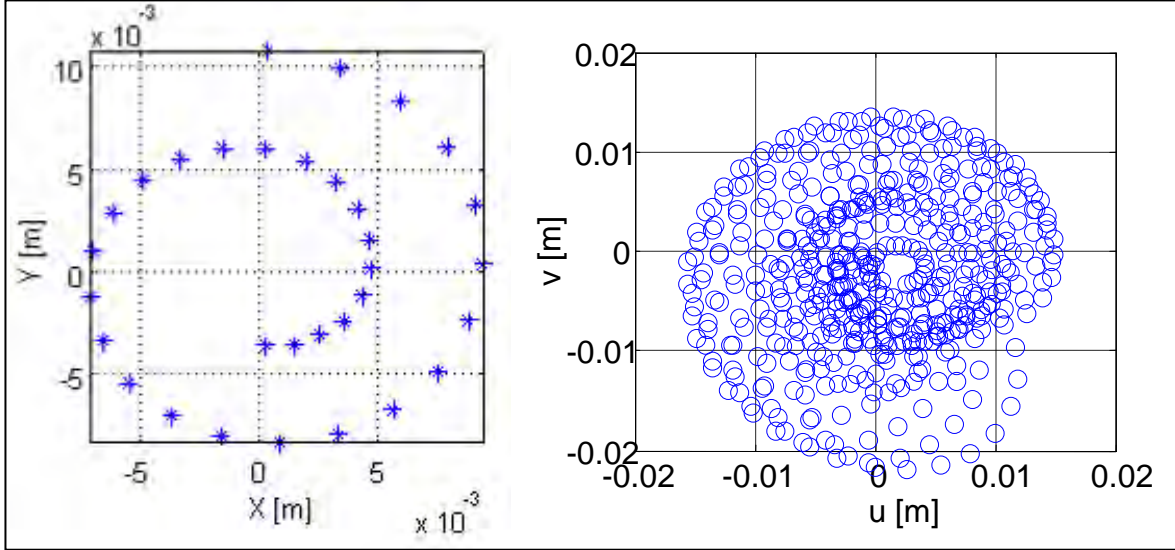


Figure 3. (Left) Array geometry showing 32 detector positions arranged in a spiral configuration, and (right) sampling in the uv plane.

While figure 3 (right) appears to be sampling the Fourier space in a non-uniform way, it is difficult to visually determine if there is redundant sampling at similar spatial frequencies. A simple check can be provided via a histogram of the baseline lengths, which appears in figure 4 (left). There are $p = 496$ baselines in this array, and the histogram contains 50 bins. It can be seen that this geometry is neither a poor choice (e.g., a rectangular gridded array, which samples relatively few spatial frequencies) nor an ideal one (in which the histogram would be nominally flat from the minimum spatial frequency to the maximum). There are exactly 490 unique baseline lengths in the array; a non-redundancy figure of merit (FOM) can be defined as the number of unique baseline lengths divided by the total number of baselines in the array. For this array, that FOM is 0.988. For comparison, figure 4 (right) contains a histogram of the baseline lengths for a rectangular-gridded array with $N = 36$ detectors (and therefore $p = 630$ baselines) and the same approximate physical size as the planar spiral array; inset is the rectangular array configuration (*cf.* figure 3 (left)). Straightforward geometry shows that there are exactly 19 unique baseline lengths in the rectangular-gridded array. The non-redundancy FOM for this array is 0.030.

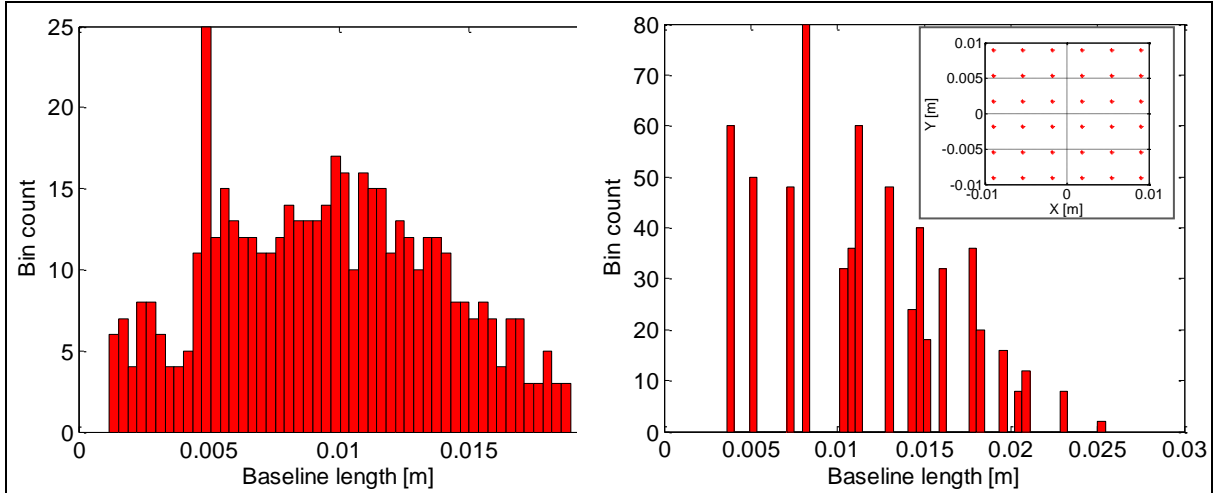


Figure 4. (Left) A histogram containing the uv plane coverage shown in Cartesian coordinates in figure 3 (right). The histogram contains 496 samples in 50 bins. (Right) A histogram showing uv plane coverage for a rectangularly-gridded array, with approximately the same number of detectors and physical size as that of figure 3 (left).

The spatial resolution of an interferometric array can be approximated by $\lambda Z_0/b$, where b is the largest baseline in the array. For the array shown in figure 3 (left), $b \approx 19$ mm. At a range of 0.5 m the spatial resolution should be approximately 3.6 cm. Figure 5 (left) shows a reconstructed amplitude distribution of a point source at 0.5 m. To verify the full-width half-maximum (FWHM) spot size, a fitting code using the Nelder-Mead direct search simplex algorithm (4) was written to find the best-fit 2-D Gaussian to the data. The general form of the 2-D Gaussian is used: $f(x, y) = A \exp[-a(x - x_0)^2 + 2b(x - x_0)(y - y_0) + c(y - y_0)^2]$, where a , b , and c are functions of both the rotation angle, and x and y Gaussian widths. Figure 5 (right) shows the results of the fitting algorithm. The mesh surface is the simulated data, while the opaque surface is the best-fit 2-D Gaussian. The mean of the x and y Gaussian widths was $\sigma \approx 0.03$ m; multiplication by $\sqrt{2 \ln 2}$ results in a FWHM of 3.55 cm, which is very close to the expected 3.6 cm.

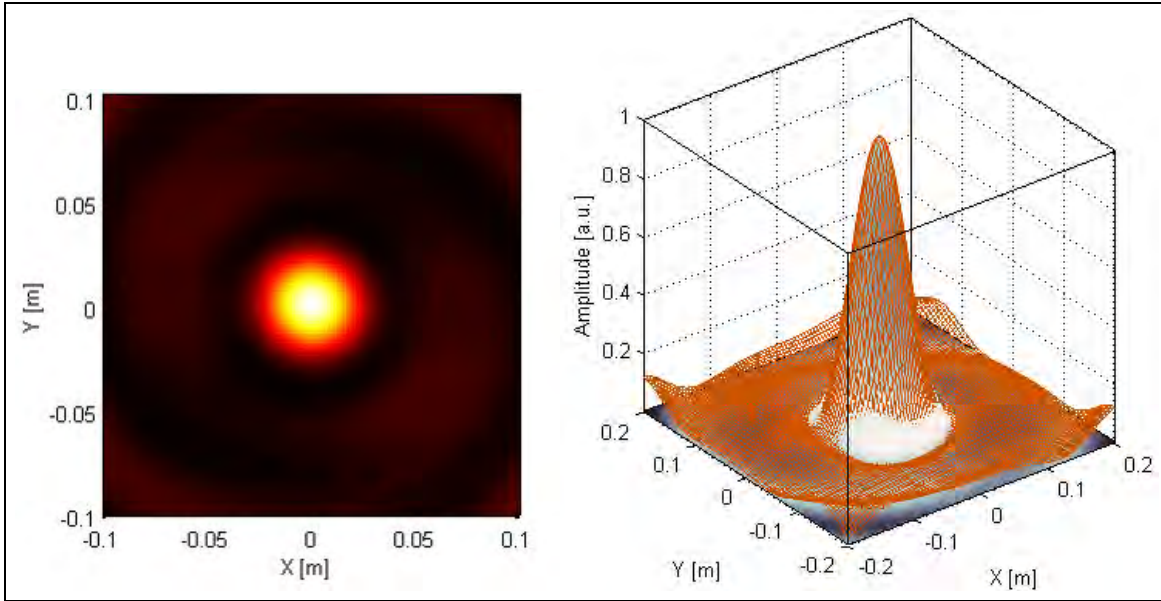


Figure 5. (Left) Reconstruction of the simulated point source at a range of 0.5 m from the spiral array, and (right) best-fit 2-D Gaussian (opaque surface) with the reconstructed object plane (mesh surface), for purposes of determining the FWHM of the point source.

Next, we investigated multiple point sources. With the same planar Archimedean spiral array and distance to the object plane, we added a second point source 6 cm above the first. The results in figure 6 show that the two sources are clearly resolved. A similar best-fit Gaussian code was developed to accommodate fitting to multiple Gaussians and was applied to the two-source simulation results.

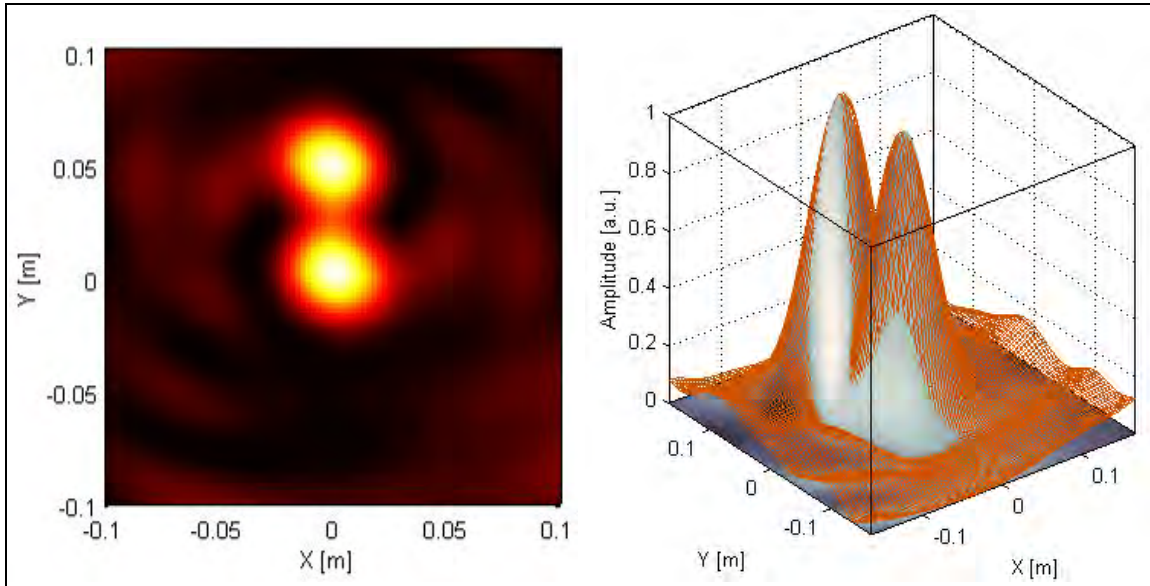


Figure 6. (Left) Reconstruction of the two simulated point sources at a range of 0.5 m from the spiral array, and (right) best-fit 2-D Gaussians (opaque surface) with the reconstructed object plane (mesh surface).

To determine if the simulation results were valid, we constructed a simple table-top experiment consisting of a 220-GHz transmitter and receiver. We installed a waveguide directional coupler at the transmitter output, and with a pair of attenuators, set the output power at both waveguides (coupled and through) to be as close to identical as possible. This measurement was performed using a calibrated substitution power meter. The spacing between the waveguide apertures was approximately 6 cm. We raster-scanned the receiver over the spatial region where the 32 detectors were modeled. The field was sampled on a square grid with a pixel dimension of 0.794 mm per side. The results are shown in figure 7 (amplitude only, phase not shown), with the nominal detector positions of the modeled Archimedean spiral overlaid. The interference pattern is slightly tilted because the waveguide apertures were not perfectly aligned with the y -axis of the experiment.

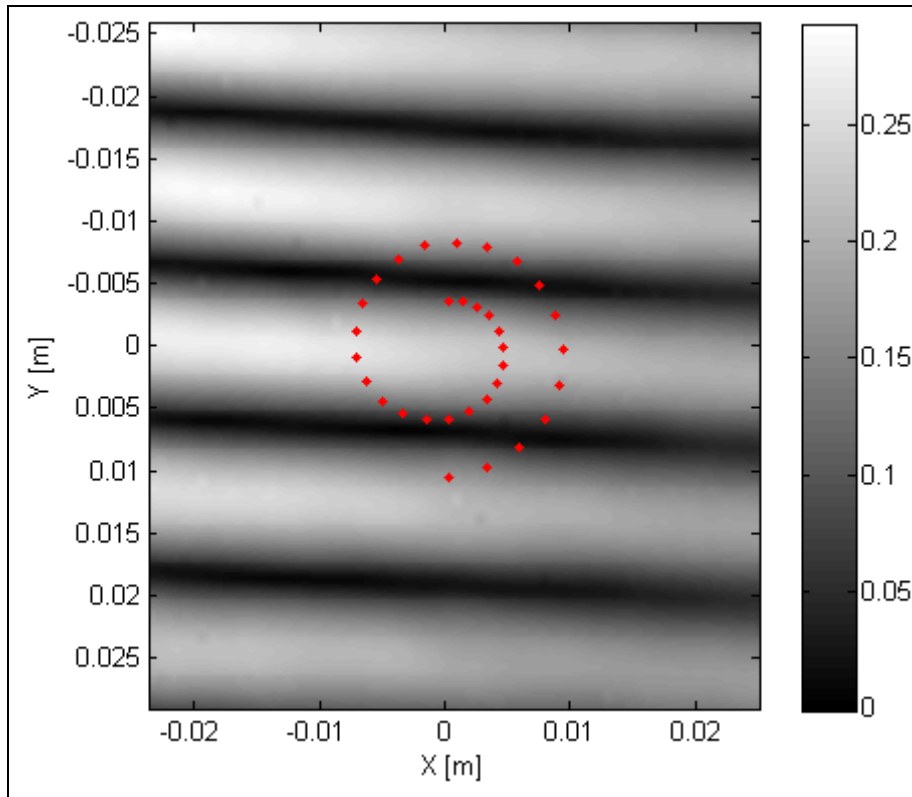


Figure 7. Measured electric field amplitude pattern of two waveguide aperture sources. Range to the sources is approximately 0.5 m, and they are separated by approximately 6 cm. The fringes are tilted slightly, as the sources were not perfectly aligned with the y -axis. The nominal positions of the modeled detectors are depicted by the overlaid dots.

The measured complex electric field was interpolated to a grid with three times more points in x and y , and then the electric field amplitude and phase were interpolated to the nearest points of the modeled spiral. This produces a 1×32 vector with a measured electric field amplitude and phase at each detector's position in the modeled spiral. This 1×32 complex vector was loaded into the MATLAB code used in the previous simulations, and the code was started at the

subroutines that process the electric field amplitude and phase from each detector. The next step in the processing is to calculate the correlation function for each baseline in the spiral as mentioned earlier, $C_l = A_l \exp(j\Delta\phi_l)$, where $A_l = E_m E_n$ is the product of the measured field amplitudes at detector locations m and n , and $\Delta\phi_l = \phi_m - \phi_n$ is the difference in phase between the two detector locations. The reconstruction result is shown in figure 8 (left).

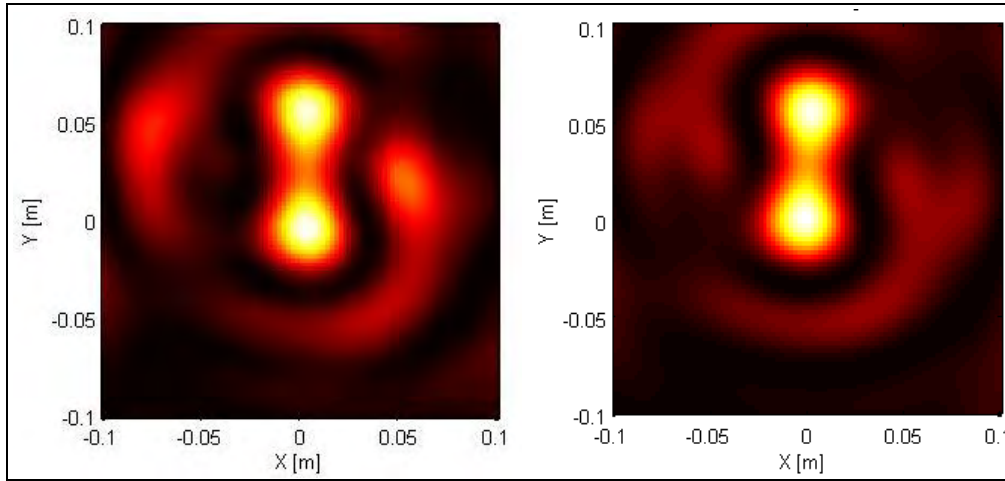


Figure 8. (Left) Measured data, reconstructed electric field distribution at object plane and (right) simulation results with geometry matching the experimental setup.

Figure 8 (right) contains the results of the same geometry, but with purely simulated data. The agreement between simulation and experiment is very good, and verifies that the concepts explained in section 3 are valid.

4. Conclusions

We explored and verified the feasibility of interferometric imaging techniques for use at millimeter-wave frequencies and short ranges. The paraxial approximation of the van Cittert-Zernike theorem that radio astronomers use is applicable in the situations described by this report, as long as the phase front curvature is compensated for. This is equivalent to re-focusing the array to the near-field, a technique that has been discussed by some in the radio astronomy community (5) for studying astronomical objects in our solar system.

5. References

1. Born, M.; Wolf, E. *Principles of Optics: Electromagnetic Theory of Propagation, Interference and Diffraction of Light*, 7th ed.; Cambridge University Press, 1999.
2. Thompson, R.; Moran, J.; Swenson, G. *Interferometry and Synthesis in Radio Astronomy*, 2 ed.; Wiley-VCH, 2001.
3. Carter, W. H. Three Different Kinds of Fraunhofer Approximations: 1. Propagation of the Field Amplitude. *Radio Science* **November–December 1988**, 23 (6), 1085–1093.
4. Lagarias, J. C.; Reeds, J. A.; Wright, M. H.; Wright, P. E. Convergence Properties of the Nelder-mead Simplex Method in Low Dimensions. *SIAM J. Optim.* **1998**, 9 (1), 112–147.
5. Carter, W. H. On Refocusing a Radio Telescope to Image Sources in the Near Field of the Antenna Array. *IEEE Trans. Antennas Prop.* **March 1989**, 37 (3), 314–319.

NO. OF COPIES	ORGANIZATION	NO. OF COPIES	ORGANIZATION
1 ELEC	ADMNSTR DEFNS TECHL INFO CTR ATTN DTIC OCP 8725 JOHN J KINGMAN RD STE 0944 FT BELVOIR VA 22060-6218	1	US ARMY RSRCH OFC ATTN RDRL ROE L D PALMER PO BOX 12211 RESEARCH TRIANGLE PARK NC 27709
1 CD	OFC OF THE SECY OF DEFNS ATTN ODDRE (R&AT) THE PENTAGON WASHINGTON DC 20301-3080	2	NAV RSRCH LAB ATTN 4820 TECHL INFO DIV ATTN 5340 E MOKOLE 4555 OVERLOOK AVE SW WASHINGTON DC 20375-5000
1 CD	OFC OF THE SECY OF DEFNS ATTN OUSD(A&T) 3080 DEFENSE PENTAGON WASHINGTON DC 20301-7100	1	US GOVERNMENT PRINT OFF DEPOSITORY RECEIVING SECTION ATTN MAIL STOP IDAD J TATE 732 NORTH CAPITOL ST NW WASHINGTON DC 20402
1	UNDER SECY OF DEFNS FOR RSRCH & ENGRG ATTN RSRCH & ADVNCD TECHLGY DEPART OF DEFNS WASHINGTON DC 20301	1	GEORGIA INST OF TECHLGY GEORGIA TECH RSRCH INST ATTN RADAR & INSTUMNTN LAB ATLANTA GA 30332
1	US ARMY RSRCH DEV AND ENGRG CMND ARMAMENT RSRCH DEV & ENGRG CTR ARMAMENT ENGRG & TECHNLY CTR ATTN AMSRD AAR AEF T J MATTS BLDG 305 ABERDEEN PROVING GROUND MD 21005-5001	1	OHIO STATE UNIV ATTN ELECT SCI LAB COLUMBUS OH 43212
1	US ARMY AMRDEC ATTN RDMR WS H EVERETT REDSTONE ARSENAL AL 35898	4	UNIV OF COLOARADO AT BOULDER DEPT ELEC CMPTR ENRGY ENG ATTN D FILIPOVIC ATTN E KUESTER ATTN J CHISUM ATTN Z POPOVIC 425 UCB BOULDER CO 80309-0245
1	US ARMY INFO SYS ENGRG CMND ATTN AMSEL IE TD A RIVERA FT HUACHUCA AZ 85613-5300	2	UNIV OF DELAWARE DEPT OF ELECT & COMP ENGRG ATTN D PRATHER ATTN M MIROZNIK EVANS HALL NEWARK DE 19716
1	COMMANDER US ARMY RDECOM ATTN AMSRD AMR W C MCCORKLE 5400 FOWLER RD REDSTONE ARSENAL AL 35898-5000	1	CALTECH/JPL ATTN MS 168-314 P SIEGEL 4800 OAK GROVE DR PASADENA CA 91109

NO. OF
COPIES ORGANIZATION

10 US ARMY RSRCH LAB
ATTN IMNE ALC HRR MAIL &
RECORDS MGMT
ATTN RDRL CIO LL TECHL LIB
ATTN RDRL CIO MT TECHL PUB
ATTN RDRL SER J MAIT
ATTN RDRL SER M A HEDDEN
ATTN RDRL SER M A ZAGHLOUL
ATTN RDRL SER M C DIETLEIN
ATTN RDRL SER M D WIKNER
ATTN RDRL SER M E ADLER
ATTN RDRL SER P AMIRTHARAJ
ADELPHI MD 20783-1197